IEEE Access
Multidisciplinary : Rapid Review : Open Access Journal

Received 15 December 2022, accepted 25 December 2022, date of publication 3 January 2023, date of current version 9 January 2023.

Digital Object Identifier 10.1109/ACCESS.2022.3233922

RESEARCH ARTICLE

3-D Analytical Model of Axial-Flux Permanent Magnet Machine With Segmented Multipole-Halbach Array

TAISHI OKITA AND HISAKO HARADA
Department of Research and Engineering, Seiko Epson Corporation, Nagano 399-0293, Japan
Corresponding author: Taishi Okita (Okita.Taishi@exc.epson.co.jp)

ABSTRACT This paper presents a 3-D analytical model of an axial-flux permanent magnet (AFPM) machine with a segmented multipole-Halbach PM array. Closed-form solutions are self-consistently derived in terms of modified Bessel functions of the first- and the second-kind by solving analytically Laplace and Poisson equations by the method of magnetic scalar potential subject to the appropriate boundary conditions. In the preceding studies, their formulations are based on a 2-D or quasi 3-D geometry, and their discussions are often limited to the magnetic fields with low-poles of the regular PM. The proposed model successfully provides more rigorous and widely applicable expressions for magnetic fields, back-electromotive force, Lorentz torque and torque constant without limitations on the number of poles and the arrangements of the PM. Behavior of the torque constant is then shown against the number of poles ranging widely from low-poles to high-poles of the regular PM, the standard-Halbach PM and the multipole-Halbach PM for changeable geometrical parameters. The obtained results are of much use in understanding intrinsically the performance characteristics of the AFPM.

INDEX TERMS Axial flux, permanent magnet, Halbach array, multipole, magnetic field, back-electromotive force, Lorentz force, torque constant.

I. INTRODUCTION

The axial-flux permanent magnet (AFPM) machine has potentially attractive features of high torque density, high efficiency and high magnetic poles due to its flat geometry in comparison to the ordinal radial flux permanent magnet (RFPM) machine. The AFPM machine has thus recently attracted great attention as a powerful candidate for a next generation driving source in many applications, e.g. robotics [1], [2], [3], [4], electric vehicles [5], [6], [7], [8] and power generation [9], [10], [11], [12]. In particular, industrial robots involving actuators have been researched and developed in the world by academic institutes [13], [14] and leading companies [15], [16], [17]. Thanks to them, man-powered heavy works have increasingly been replaced and automated by the robots. In multi-jointed robots, the performance required for servomotors ranges widely from high-revolution to high-torque, depending on the role of each joint. Specifically, a quick response is demanded for the joint close to the point of action, where low-pole and high-revolution RFPM would be suitable. On the other hand, a large load is inevitably applied on the joint corresponding to the point of effort, where multipole and high-torque AFPM would be effective. In either case, the basic performance of the PM machines is almost characterized by the torque constant. It is therefore very important to understand characteristics of the torque constant of the AFPM as well as the RFPM over a global range of the various designing parameters.

In order to generate high torque in electric machines, a Halbach PM array has so far been suggested and studied in various areas by many researchers [18], [19], [20], [21], [22], [23], [24]. The Halbach array is superior to ordinal one in several ways; First, the Halbach PM produces an about twice stronger magnetic flux density than ordinal one. Second,

The associate editor coordinating the review of this manuscript and approving it for publication was Xiaodong Liang.

the magnetic field distribution is approximately sinusoidal. Third, the leakage flux from back side is almost negligible. These advantages are expected to be enhanced for a multipole-Halbach array with higher poles by the interaction of magnetic fields in the adjacent magnets. However, characteristics of the AFPM with a multipole-Halbach PM has not yet sufficiently been studied in comparison with those of the RFPM, and most of previous studies have been confined to the low number of poles because of the facility in modeling, designing and manufacturing.

In designing high performance machines, it is of intrinsic importance to study magnetic field structures in the air-gap and their Fourier spectra, since the fundamental amplitude of the fields produces the net Lorentz force by interacting synchronously with the alternating electric current of the coil, while the harmonics results in the ineffective force such as cogging torque and/or torque ripple. Most preceding works utilize commercially available simulation programs, in which electromagnetic (EM) fields are numerically solved by, e.g. the finite element method (FEM) [25], [26], [27]. However, such a numerical method requires enormous computation time for a 3-D structure of the AFPM, and makes the principle governing underlying physics unclear. Furthermore, the FEM analysis forces us to remodel every time the geometrical parameters, e.g. the number of poles and/or the arrangements of the PM change, and the computation accuracy becomes unstable for higher poles. For these reasons, the FEM is not suitable for a global parametrical study on the 3-D AFPM model. This work therefore adopts an analytical approach, which makes it possible to investigate EM problems not only quickly, but also flexibly, and then to provide deep physical insight through mathematical formulations.

Pioneering analytical studies on the AFPM can be found in the literature [28], [29], in which magnetic fields in the air-gap have been investigated by integrating the free-space Green function. Magnetic fields of the disk-type PM have also been analyzed by taking the Hankel transformation [30]. However, these preceding papers are limited to the study only on the magnetic field structure itself of the regular PM array with low-poles. 2-D analytical studies of the AFPM have been reported in [31] and [32], which provide the relevant solutions formulated in terms of a vector potential by introducing an artificial correction function in the radial direction. Such a 2-D approximate model would be valid only when the inner radius is close to the outer one. 3-D analytical models of the ironless AFPM machine have been suggested in [33], [34], in which magnetic fields are studied only for the regular PM array with low-poles, and torque characteristics is not reported. In a similar paper [35], magnetic fields and the relevant torque have also been analyzed on the basis of a 3-D AFPM model with a standard-Halbach PM, but high-order space harmonics are neglected in their torque formula, and the results are limited to a single case of low-poles. A complete 3-D model of the AFPM is therefore highly required in order to investigate systematically magnetic fields, back electromotive force(EMF) and torque characteristics without limitation on the regular PM with low-poles.

From a theoretical point of view, in the existing papers, e.g. [33] and [34] basic solutions have been given in the single form of the first-kind Bessel function under the open-circuit condition in order to avoid complicated formulations. Their formulae actually include only one unknown quantity to be determined by the boundary condition. This work is different from the preceding ones in that general solutions have more rigorously been derived and expressed in the combination of the first- and the second-kind modified Bessel functions by solving straightforwardly Laplace and Poisson equations in the air-gap and the magnet regions, respectively. Our formulae thus involve six unknowns to be determined by the appropriate boundary conditions. The novelty of this work lies in the fact that the proposed model successfully provides more rigorous and widely applicable mathematical expressions for magnetic fields, back-EMF, Lorentz torque and torque constant without limitations on the number of poles and the arrangements of the PM. To the best of the authors' knowledge, such a rigorous formula for the torque constant based on the 3-D multipole-Halbach AFPM has not been found in the preceding papers. The objective of this paper is to derive analytically an expression for the torque constant, and to show its dependence on the number of poles ranging widely from low-poles to high-poles for geometrical parameters of the multipole-Halbach AFPM. In addition, the proposed model enables us to study rapidly EM characteristics of the AFPM, incorporating the effect of high-order space harmonics without sacrificing a degree of accuracy, even if the number of poles is as high as ~ 100.

This paper is organized as follows. In Section II, geometries of the proposed model are presented. In Section III, basic equations are self-consistently formulated, and then the rigorous expressions for magnetic fields, back-EMF, Lorentz torque and torque constant are successfully derived. Section IV focuses on the validity, results and discussion. Finally, Section V summarizes this work.

II. MODEL

Fig.1a) presents the analytical 3-D model of the AFPM machine developed in this work, where R_o and R_s are inner and outer radii of the stator core, R_r and R_m are inner and outer radii of the rotor magnet, respectively, g is a mechanical air-gap, z_m is a thickness of the magnet in the axial direction, Δ is an angle spread by a segment arc, θ_c is an angle spread by a coil arc, and θ_s is a coil-pitch. This model comprises of four assembly: a rotor magnet, a back yoke, three-phase (U,V,W) coils, and a slotless stator.

This figure is illustrated for changeable parameters $p = 2$, $Q = 6$ and $l = 2$ as one of the examples, where p is the number of pole-pairs, Q is the number of coils, and l is the number of segments per pole. Throughout the paper, the machine is driven by three-phase sinusoidally alternating electric currents, and the ratio of the pole-pairs and the number of coils is chosen to be the most popular combination $Q/(2p) = 3/2$. All of the magnet pieces are sequentially assigned with number $i = 1, 2, \cdots, 2pl$, and all of the coils are similarly numbered as $j = 1, 2, \cdots, Q$ in the order of U, V and W phases. The analysis regions are divided into three regions, Ω_1, Ω_2 and Ω_3, as shown in the figure. In this model, $l = 1$ corresponds to an ordinal PM, $l = 2$ to a standard-Halbach PM, $l \geq 3$ to segmented multipole-Halbach PMs, and $l \gg 1$ approaches an ideal Halbach PM, as shown in Fig.1b).

This work is based on the following assumptions; First, permeability of the stator yoke and the magnet yoke is infinite, in other words magnetic saturation in the yoke is negligible. Second, thickness of the coil is neglected, that is to say, delta-function coil is adopted. Third, effects of the eddy current, e.g. Joule heat in the yoke and/or magnetic coupling between the rotor and the stator, are not incorporated. Fourth, secondary magnetic fields coming from the electric current of the coil is much weaker than those of the magnet. Fifth, the PM has a linear magnetization characteristics with a constant remanence and a constant recoil permeability. The effect of demagnetization is thus not considered in the model. It is also important to study such nonlinear complicated effects in a practical stage of designing and/or manufacturing, but is beyond the scope of this paper.

III. FORMULATION

A. MAGNETIC FIELDS

The governing equations for magnetostatic fields $\boldsymbol{B}$ and $\boldsymbol{H}$ are self-consistently formulated as

$$\nabla \cdot \boldsymbol{B} = 0 \qquad \text{in all regions} \tag{1}$$

$$\nabla \times \boldsymbol{H} = 0 \qquad \text{in all regions} \tag{2}$$

$$\boldsymbol{B} = \mu_0 \boldsymbol{H} \qquad \text{in } \Omega_1 \text{ and } \Omega_3 \tag{3}$$

$$\boldsymbol{B} = \mu_0 \mu_\mathrm{r} \boldsymbol{H} + \mu_0 \boldsymbol{M} \qquad \text{in } \Omega_2 \tag{4}$$

where $\boldsymbol{M}$ is a magnetization vector of the PM, $\mu_0 = 4\pi \times 10^{-7}$ H/m is a permeability of the vacuum, and μ_r is a relative recoil permeability of the PM.

As shown in Fig.2, the magnetization vector $\boldsymbol{M}_i$ for the i-th segment of the PM with an array variable l can be expressed in a cylindrical coordinates system (r, θ, z) as

$$\boldsymbol{M}_i = M_{i,r}\boldsymbol{e}_r + M_{i,\theta}\boldsymbol{e}_\theta + M_{i,z}\boldsymbol{e}_z \tag{5}$$

where

$$M_{i,r} = M_i \cos\varphi_i \sin(\theta - \vartheta_i) \tag{6}$$

$$M_{i,\theta} = M_i \cos\varphi_i \cos(\theta - \vartheta_i) \tag{7}$$

$$M_{i,z} = M_i \sin\varphi_i \tag{8}$$

and $\varphi_i \equiv \pi(i-1)/l + \pi/2$ is an elevation angle of the magnetization vector, $\vartheta_i \equiv \pi(i-1)/(pl)$ is an azimuthal angle measured from the x-axis to the line extended radially from the origin O through the center G_i, $\boldsymbol{e}_r, \boldsymbol{e}_\theta$ and $\boldsymbol{e}_z$ are unit vectors in the radial, azimuthal and axial direction, respectively. It is worth noting that magnetization pattern of the PM can exactly be realized through the elevation angle φ_i and the azimuthal angle ϑ_i by substituting integers into the array parameter l.

Magnetic scalar potential $\phi = \phi(r, \theta, z)$ can now be introduced because of the curl-free relation (2) as

$$H_r = -\frac{\partial \phi}{\partial r}, \quad H_\theta = -\frac{1}{r}\frac{\partial \phi}{\partial \theta}, \quad H_z = -\frac{\partial \phi}{\partial z}. \tag{9}$$

Taking divergence of (3) and (4) in combination with (1) provides Laplace and Poisson equations, respectively

$$\frac{\partial^2 \phi}{\partial r^2} + \frac{1}{r}\frac{\partial \phi}{\partial r} + \frac{\partial^2 \phi}{\partial \theta^2} + \frac{\partial^2 \phi}{\partial z^2} = 0 \quad \text{in } \Omega_1 \text{ and } \Omega_3 \tag{10}$$

$$\frac{\partial^2 \phi}{\partial r^2} + \frac{1}{r}\frac{\partial \phi}{\partial r} + \frac{\partial^2 \phi}{\partial \theta^2} + \frac{\partial^2 \phi}{\partial z^2} = \frac{1}{\mu_\mathrm{r}} \nabla \cdot \boldsymbol{M} \quad \text{in } \Omega_2. \tag{11}$$

General solution for the Laplace equation (10) can be expanded in the form of double-Fourier series in the manner of separation of variables as

$$\phi = \sum_{n=\mathrm{odd}}^{\infty} \sum_{k=1}^{\infty} X_{nk}(x) \cos(\nu\theta) \sin(\lambda z) \tag{12}$$

where $\nu \equiv np$, $\lambda \equiv 2k\pi/\tau$, $\tau \equiv 2z_\mathrm{s}$, and X_{nk} are the specific functions to be determined below in each region in terms of the normalized radial coordinate, $x \equiv \lambda r$.

Components of the magnetization vector can similarly be expressed as

$$M_r \simeq 0 \tag{13}$$

$$M_\theta = \sum_{n=\mathrm{odd}}^{\infty} \sum_{k=1}^{\infty} M_{\theta nk} \sin(\nu\theta) \sin(\lambda z) \tag{14}$$

$$M_z = \sum_{n=\mathrm{odd}}^{\infty} M_{zn0} \cos(\nu\theta) + \sum_{n=\mathrm{odd}}^{\infty} \sum_{k=0}^{\infty} M_{znk} \cos(\nu\theta) \cos(\lambda z) \tag{15}$$

where

$$M_{\theta nk} = \frac{8p}{\pi\tau} \int_0^{\pi/p} d\theta \int_0^{\tau/2} dz M_\theta(\theta, z) \sin(\nu\theta) \sin(\lambda z) = \frac{2N_{\theta n}}{k\pi} \left\{1 - \cos\left(\alpha_\mathrm{q} k\pi\right)\right\} \tag{16}$$

$$N_{\theta n} \equiv \frac{M}{2} \left\{ sinc\psi_{\nu_n} + sinc\psi_{-\nu_n} \right\} (\delta_{n,2\kappa l-1} - \delta_{n,-2\kappa' l+1}) \tag{17}$$

$$\psi_{\nu_n} \equiv (1+\nu)\Delta/2 \qquad (\kappa = 1, 2, \cdots; \kappa\prime = 0, -1, \cdots) \tag{18}$$

and

$$M_{znk} = \frac{8p}{\pi\tau} \int_0^{\pi/p} d\theta \int_0^{\tau/2} dz M_z(\theta, z) \cos(\nu\theta) \cos(\lambda z) = \frac{2M_{zn}}{k\pi} \sin(\alpha_\mathrm{q} k\pi) \tag{19}$$

$$M_{zn} \equiv M sinc\chi_{\nu_n} (\delta_{n,2\kappa l-1} + \delta_{n,-2\kappa' l+1}) \tag{20}$$

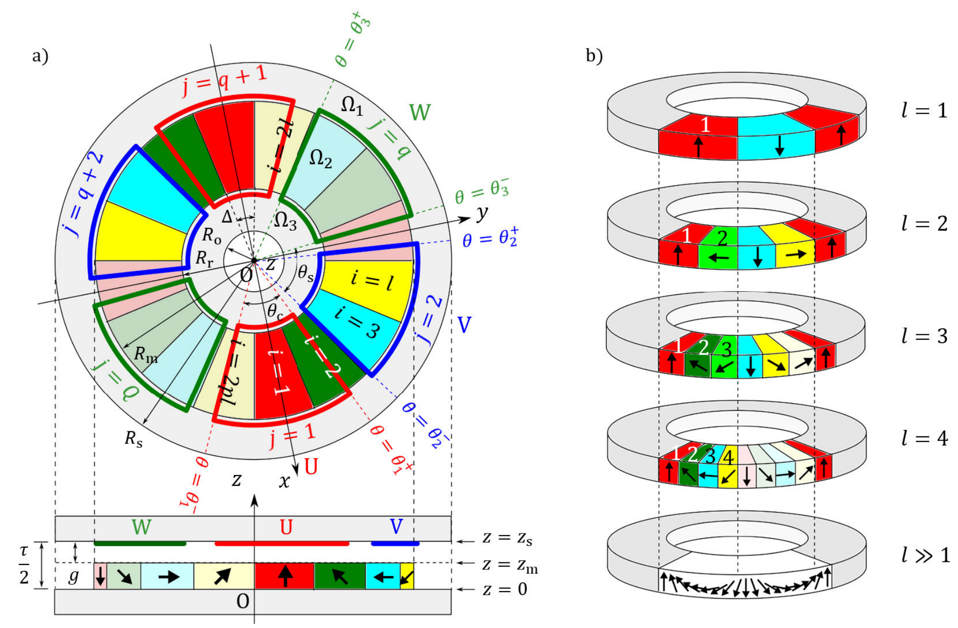

FIGURE 1. a) Top view and side view of the analytical AFPM model is illustrated for changeable parameters $2p = 4$, $Q = 6$ and $l = 4$ as one of the examples. b) Arrangements of the PM with $l = 1$(regular), $l = 2$(standard-Halbach), $l = 3, 4$(multipole-Halbach) and $l \gg 1$(ideal Halbach).

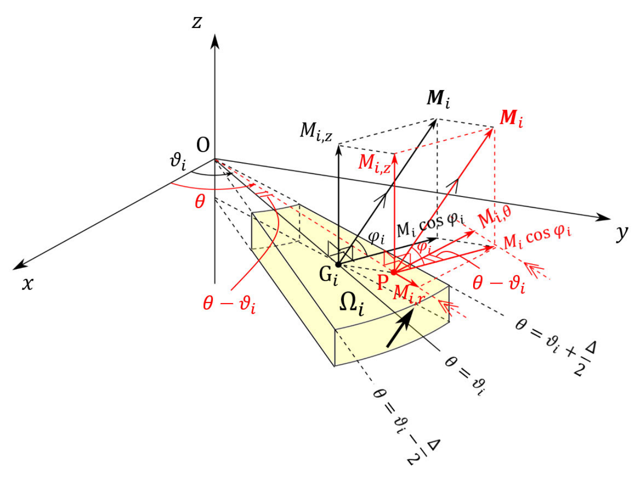

FIGURE 2. Magnetization vector M_i of the i-th PM segment with an arbitrary array parameter l. The vector M_i is uniform in each segment. See also equations (5) to (8) for more strict definitions.

$$\chi_{\nu_n} \equiv \nu\Delta/2 \quad (\kappa = 1, 2, \cdots; \kappa\prime = 0, -1, \cdots) \tag{21}$$

with $\alpha_q \equiv z_m/z_s$ and $\delta_{nm} = 1\,(n = m)$ or $0\,(n \neq m)$ a Kronecker delta notation. The radial component M_r can safely be dropped because it does not contribute to the net Lorentz torque.

The Laplace and Poisson equations (10) and (11) can therefore be rewritten in terms of the specific functions $X_{nk}(x)$ as

$$\frac{\partial^2 X_{nk}}{\partial x^2} + \frac{1}{x}\frac{\partial X_{nk}}{\partial x} - \left(1 + \frac{\nu^2}{x^2}\right) X_{nk} = 0 \quad \text{in } \Omega_{1,3} \tag{22}$$

$$\times \frac{\partial^2 X_{nk}}{\partial x^2} + \frac{1}{x}\frac{\partial X_{nk}}{\partial x} - \left(1 + \frac{\nu^2}{x^2}\right) X_{nk} = \frac{1}{\lambda}\left(\frac{\nu M_{\theta nk}}{x} - M_{znk}\right) \quad \text{in } \Omega_2. \tag{23}$$

The general solutions in the regions Ω_1, Ω_2 and Ω_3 can now respectively be expressed by

$$X_{1,nk} = A_{nk} I_\nu(x) + B_{nk} K_\nu(x) \tag{24}$$
$$X_{2,nk} = \tilde{C}_{nk}(x) I_\nu(x) + \tilde{D}_{nk}(x) K_\nu(x) \tag{25}$$
$$X_{3,nk} = E_{nk} I_\nu(x) + F_{nk} K_\nu(x) \tag{26}$$

where $I_\nu(x)$ and $K_\nu(x)$ are modified Bessel functions of the first- and the second-kind for the ν-th order, respectively, and other notations are defined by

$$\tilde{C}_{nk}(x) \equiv C_{nk} + f_{nk}(x) \tag{27}$$
$$\tilde{D}_{nk}(x) \equiv D_{nk} + g_{nk}(x) \tag{28}$$

and

$$f_{nk}(x) \equiv \frac{1}{\lambda}\int_{x_r}^{x} dx' \left(\nu M_{\theta nk} - x' M_{znk}\right) K_\nu(x') \tag{29}$$
$$g_{nk}(x) \equiv -\frac{1}{\lambda}\int_{x_r}^{x} dx' \left(\nu M_{\theta nk} - x' M_{znk}\right) I_\nu(x') \tag{30}$$

with $x_r \equiv \lambda R_r$. See also Appendix A for the relevant derivations.

Six unknown coefficients A_{nk}, B_{nk}, C_{nk}, D_{nk}, E_{nk} and F_{nk} have to be determined subject to the following boundary conditions:

$$B_{1r}(R_s, \theta, z) = 0 \tag{31}$$
$$H_{1\theta}(R_m, \theta, z) = H_{2\theta}(R_m, \theta, z) \tag{32}$$

$$B_{1r}(R_{\rm m},\theta,z) = B_{2r}(R_{\rm m},\theta,z) \tag{33}$$
$$H_{1z}(R_{\rm m},\theta,z) = H_{2z}(R_{\rm m},\theta,z) \tag{34}$$
$$H_{2\theta}(R_{\rm r},\theta,z) = H_{3\theta}(R_{\rm r},\theta,z) \tag{35}$$
$$B_{2r}(R_{\rm r},\theta,z) = B_{3r}(R_{\rm r},\theta,z) \tag{36}$$
$$H_{2z}(R_{\rm r},\theta,z) = H_{3z}(R_{\rm r},\theta,z) \tag{37}$$
$$B_{3r}(R_{\rm o},\theta,z) = 0. \tag{38}$$

The boundary condition (34) is intrinsically equivalent to (32), and (37) to (35) likewise. The number of equations to be solved therefore amounts to six. It should also be noted that the relations (31) and (38) provide Dirichlet boundary conditions at the outer edge $r = R_{\rm s}$ and the inner edge $r = R_{\rm o}$ of the yoke, while that the form of the solution (12) naturally satisfies Neumann boundary conditions $\phi(x,\theta,z=0) = \phi(x,\theta,z=z_{\rm s}) = 0$ at the upper surface $z = 0$ of the lower yoke and the lower surface $z = z_{\rm s}$ of the upper yoke. After algebraic manipulation, the above relations (31) to (38) yield

$$C_{nk} = -d^{-1}\left(\beta'_\nu K_{\nu,\rm r} + \beta_\nu \tilde{K}_{\nu,\rm r}\right)\left(\alpha'_\nu R_{nk,\rm m} - \alpha_\nu \tilde{R}_{nk,\rm m}\right) \tag{39}$$

$$D_{nk} = d^{-1}\left(\beta'_\nu I_{\nu,\rm r} - \beta_\nu \tilde{I}_{\nu,\rm r}\right)\left(\alpha'_\nu R_{nk,\rm m} - \alpha_\nu \tilde{R}_{nk,\rm m}\right) \tag{40}$$

$$d \equiv \left(\alpha'_\nu I_{\nu,\rm m} - \alpha_\nu \tilde{I}_{\nu,\rm m}\right)\left(\beta'_\nu K_{\nu,\rm r} + \beta_\nu \tilde{K}_{\nu,\rm r}\right) + \left(\alpha'_\nu K_{\nu,\rm m} + \alpha_\nu \tilde{K}_{\nu,\rm m}\right)\left(-\beta'_\nu I_{\nu,\rm r} + \beta_\nu \tilde{I}_{\nu,\rm r}\right) \tag{41}$$

where

$$\alpha_\nu \equiv \tilde{K}_{\nu,\rm s}\tilde{I}^{-1}_{\nu,\rm s} I_{\nu,\rm m} + K_{\nu,\rm m}, \quad \alpha'_\nu \equiv \tilde{K}_{\nu,\rm s}\tilde{I}^{-1}_{\nu,\rm s}\tilde{I}_{\nu,\rm m} - \tilde{K}_{\nu,\rm m} \tag{42}$$

$$\beta_\nu \equiv I_{\nu,\rm r} + \tilde{I}_{\nu,\rm o}\tilde{K}^{-1}_{\nu,\rm o} K_{\nu,\rm r}, \quad \beta'_\nu \equiv \tilde{I}_{\nu,\rm r} - \tilde{I}_{\nu,\rm o}\tilde{K}^{-1}_{\nu,\rm o}\tilde{K}_{\nu,\rm r} \tag{43}$$

$$R_{nk,\rm m} \equiv f_{nk,\rm m} I_{\nu,\rm m} + g_{nk,\rm m} K_{\nu,\rm m} \tag{44}$$
$$\tilde{R}_{nk,\rm m} \equiv f_{nk,\rm m}\tilde{I}_{\nu,\rm m} - g_{nk,\rm m}\tilde{K}_{\nu,\rm m} \tag{45}$$
$$\tilde{I}_{\nu,\rm i} \equiv I_{\nu-1,\rm i} + I_{\nu+1,\rm i}, \quad \tilde{K}_{\nu,\rm i} \equiv K_{\nu-1,\rm i} + K_{\nu+1,,\rm i} \tag{46}$$
$$I_{\nu,\rm i} \equiv I_\nu(x_{\rm i}), \quad K_{\nu,\rm i} \equiv K_\nu(x_{\rm i}) \tag{47}$$
$$f_{nk,\rm i} \equiv f_{nk}(x_{\rm i}), \quad g_{nk,\rm i} \equiv g_{nk}(x_{\rm i}) \tag{48}$$

with $x_{\rm i} \equiv \lambda_k R_{\rm i}(\rm i = o,r,m,s)$. Other coefficients are given by

$$B_{nk} = \alpha_\nu^{-1}\left(C_{nk} I_{\nu,\rm m} + D_{nk} K_{\nu,\rm m} + R_{nk,\rm m}\right) \tag{49}$$
$$E_{nk} = \beta_\nu^{-1}\left(C_{nk} I_{\nu,\rm r} + D_{nk} K_{\nu,\rm r}\right) \tag{50}$$
$$A_{nk} = B_{nk}\tilde{K}_{\nu,\rm s}\tilde{I}_{\nu,\rm s^{-1}} \tag{51}$$
$$F_{nk} = E_{nk}\tilde{I}_{\nu,\rm o}\tilde{K}^{-1}_{\nu,\rm o}. \tag{52}$$

Practical technique for numerically computing the coefficients C_{nk} and D_{nk} is given in Appendix B.

The resultant magnetic fields in the air-gap can consequently be expressed as

$$B_r = -\mu_0 \frac{\partial \phi}{\partial r} = -\mu_0 \sum_{n=\rm odd}^{\infty}\sum_{k=1}^{\infty} \lambda \frac{\partial X_{2,nk}}{\partial x}\cos(\nu\theta)\sin(\lambda z) \tag{53}$$

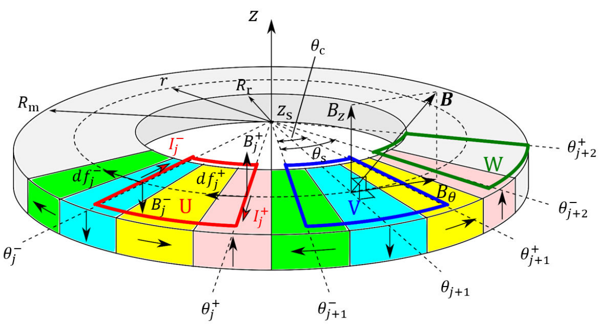

FIGURE 3. Reference geometry of the AFPM with $l = 2$ for calculating back-EMF, Lorentz force and torque.

$$B_\theta = -\mu_0 \frac{\partial \phi}{r\partial \theta} = \mu_0 \sum_{n=\rm odd}^{\infty}\sum_{k=1}^{\infty} \nu\lambda \frac{X_{2,nk}}{x}\sin(\nu\theta)\sin(\lambda z) \tag{54}$$

$$B_z = -\mu_0 \frac{\partial \phi}{\partial z} = -\mu_0 \sum_{n=\rm odd}^{\infty}\sum_{k=1}^{\infty} \lambda X_{2,nk}\cos(\nu\theta)\cos(\lambda z). \tag{55}$$

B. BACK-EMF

When the PM rotor revolves around a z-axis with a uniform angular frequency ω, the axial component B_z of the magnetic field permeating a coil surface located at $z = z_{\rm s}$ is given by

$$B_z(r,\theta,z=z_{\rm s},t) = \mu_0 \sum_{n=\rm odd}^{\infty}\sum_{k=1}^{\infty}(-1)^{k+1}\lambda X_{2,nk}\cos\nu(\theta-\omega t). \tag{56}$$

As shown in Fig.3, the linkage flux Φ_j for the j-th coil can straightforwardly be obtained by taking the surface integral for B_z over the area S_j of the coil as

$$\begin{aligned}\Phi_j &\equiv \iint_{S_j} dS B_z(r,\theta,z=z_{\rm s},t) \\ &= \mu_0 \sum_{n=\rm odd}^{\infty}\sum_{k=1}^{\infty}\frac{(-1)^{k+1}}{\lambda}\mathscr{I}_{nk}\int_{\theta_j^-}^{\theta_j^+} d\theta\cos\nu(\theta-\omega t) \\ &= 2\mu_0 \sum_{n=\rm odd}^{\infty}\sum_{k=1}^{\infty}\frac{(-1)^{k+1}}{\nu\lambda}\mathscr{I}_{nk}\sin\left(\frac{\nu\theta_{\rm c}}{2}\right) \\ &\quad \times \cos\nu(\theta_j-\omega t)\end{aligned} \tag{57}$$

where $\theta_j^\pm \equiv \theta_{\rm s}(j-1) + \pi/(2p) \pm \theta_{\rm c}/2$ correspond to both edges oriented in the radial direction of the j-th coil, and the specific integral $\mathscr{I}_{nk}$ defined by

$$\mathscr{I}_{nk} \equiv \int_{x_{\rm r}}^{x_{\rm m}} x dx X_{2,nk} \tag{58}$$

reflects the magnetic field structure in the radial direction. The back-EMF $\mathcal{E}_j$ in the j-th coil is now induced by the time-varying flux according to the Lenz's law

$$\mathcal{E}_j = -N_c \frac{\partial \Phi_j}{\partial t} = -2\mu_0 N_c \omega \sum_{n=\text{odd}}^{\infty} \sum_{k=1}^{\infty} \frac{(-1)^{k+1}}{\lambda} \mathscr{I}_{nk} \sin\left(\frac{\nu\theta_c}{2}\right) \times \sin \nu(\theta_j - \omega t) \tag{59}$$

where N_c is the number of turns in a coil, and hereafter $N_c = 1$ for simplicity. The relevant line back-EMF between the U- and V-phase is then obtained by taking difference between the phase back-EMFs with $j = 1$ and 2

$$\mathcal{E}_2 - \mathcal{E}_1 = -4\mu_0 \omega \sum_{n=\text{odd}}^{\infty} \sum_{k=1}^{\infty} \frac{(-1)^{k+1}}{\lambda} \mathscr{I}_{nk} \times \sin\left(\frac{\nu\theta_c}{2}\right) \sin\left(\frac{n\pi}{q}\right) \cos\left(\frac{2+q}{2q} n\pi - \nu\omega t\right) \tag{60}$$

where $q(= 3)$ represents the number of phases.

C. LORENTZ FORCE AND TORQUE

Let us now formulate Lorentz force and torque. In this paper, the Lorentz torque is defined as the moment of force that purely derives from the Lorentz force oriented in the circumferential (θ) direction. As shown in Fig.3, the Lorentz force df_j exerted on an infinitesimal current element $I_j dr$ of the j-th coil is given by

$$df_j = (B_j^+ - B_j^-) I_j dr, \tag{61}$$

where $B_j^\pm \equiv B_z(r, \theta_j^\pm, z = z_s, t)$ are axial magnetic fields at both edges of the j-coil, and $I_j \equiv I_0 \cos p(\omega t - \delta_j)$ is an electric current in the j-th coil with I_0 a peak current and $\delta_j \equiv 2\pi(j-1)/(pq)$ a phase shift. The Lorentz force df per pole-pair is driven by a set of the U-, V- and W-phase coils, and is expressed as

$$df \equiv \sum_{j=1}^{q} df_j = -2\mu_0 I_0 dr \sum_{j=1}^{q} \sum_{n=\text{odd}}^{\infty} \sum_{k=1}^{\infty} (-1)^{k+1} \lambda X_{2,nk} \times \sin\left(\frac{\nu\theta_c}{2}\right) \cos p(\omega t - \delta_j) \sin \nu(\theta_j - \omega t). \tag{62}$$

Noticing the explicit relation

$$\sin \nu(\theta_j - \omega t) = (-1)^{\frac{n-1}{2}} \cos \nu(\theta_j' - \omega t) \tag{63}$$

one obtains

$$df = 2\mu_0 I_0 dr \sum_{j=1}^{q} \sum_{n=\text{odd}}^{\infty} \sum_{k=1}^{\infty} (-1)^{\frac{2k+n+1}{2}} \lambda X_{2,nk} \times \cos p(\omega t - \delta_j) \cos \nu(\omega t - \theta_j') \tag{64}$$

with $\theta_j' \equiv \theta_s(j-1)$. Taking the following identity of the summation in terms of j

$$2\sum_{j=1}^{q} \cos p\omega t \cos \nu(\omega t - \theta_j') = \cos\phi_n \sum_{j=1}^{q} \cos\psi_{n,j} + \cos\phi_{-n} \sum_{j=1}^{q} \cos\psi_{-n,j} \tag{65}$$

the formula (64) reduces to

$$\frac{1}{\mu_0 I_0 q} \frac{df}{dr} = \frac{1}{q} \sum_{j=1}^{q} \sum_{n=\text{odd}}^{\infty} \sum_{k=1}^{\infty} (-1)^{\frac{2k+n+1}{2}} \lambda X_{2,nk} \sin\left(\frac{\nu\theta_c}{2}\right) \times \left(\cos\phi_n \sum_{j=1}^{q} \cos\psi_{n,j} + \cos\phi_{-n} \sum_{j=1}^{q} \cos\psi_{-n,j}\right) \tag{66}$$

where $\phi_n(t) \equiv (1+n)p\omega t$ and $\psi_{n,j} \equiv 2\pi(1+n)(j-1)/q$. The Lorentz torque T can finally be obtained by the integration with respect to $dT \equiv r df$ as

$$T = \int dT = \mu_0 I_0 \sum_{n=\text{odd}}^{\infty} \sum_{k=1}^{\infty} (-1)^{\frac{2k+n+1}{2}} \lambda^{-1} \times \mathscr{I}_{nk} (\xi_n \cos\phi_n + \xi_{-n} \cos\phi_{-n}) \sin\left(\frac{\nu\theta_c}{2}\right) \tag{67}$$

where we have used the relation

$$\xi_n \equiv \sum_{j=1}^{q} \cos\psi_{n,j} = 1 - (-1)^n \left(\cos\frac{n\pi}{q} - \sqrt{3}\sin\frac{n\pi}{q}\right). \tag{68}$$

Eigen modes and eigen frequencies are summarized in Table 1, where nontrivial modes are indicated by bold letters. Trivial modes do not generate the net Lorentz force. The Lorentz torque can therefore be expanded in terms of the nontrivial modes as follows

$$\begin{aligned}
\frac{1}{\mu_0 I_0 q} T &= \sum_{k=1}^{\infty} \frac{(-1)^{k+1}}{\lambda} \mathscr{I}_{1k} \sin\Theta_1 \\
&+ \sum_{k=1}^{\infty} \frac{(-1)^{k+3}}{\lambda} (\mathscr{I}_{5k} \sin\Theta_5 - \mathscr{I}_{7k} \sin\Theta_7) \cos\phi_5 \\
&+ \sum_{k=1}^{\infty} \frac{(-1)^{k+6}}{\lambda} (\mathscr{I}_{11k} \sin\Theta_{11} - \mathscr{I}_{13k} \sin\Theta_{13}) \cos\phi_{11} \\
&+ \sum_{k=1}^{\infty} \frac{(-1)^{k+9}}{\lambda} (\mathscr{I}_{17k} \sin\Theta_{17} - \mathscr{I}_{19k} \sin\Theta_{19}) \cos\phi_{17} \\
&+ \cdots
\end{aligned} \tag{69}$$

TABLE 1. Eigen modes and eigen frequencies.

n	ϕ_n	ϕ_{-n}	$\Psi_{n,j}$	$\Psi_{-n,j}$
1	$2p\omega t$	$\mathbf{0}$	$4\pi/3(j-1)$	$\mathbf{0}$
3	$4p\omega t$	$-2p\omega t$	$8\pi/3(j-1)$	$-4\pi/3(j-1)$
5	$\boldsymbol{6p\omega t}$	$-4p\omega t$	$\boldsymbol{4\pi(j-1)}$	$-8\pi/3(j-1)$
7	$8p\omega t$	$\boldsymbol{-6p\omega t}$	$16\pi/3(j-1)$	$\boldsymbol{-4\pi(j-1)}$
9	$10p\omega t$	$-8p\omega t$	$20\pi/3(j-1)$	$-16\pi/3(j-1)$
11	$\boldsymbol{12p\omega t}$	$-10p\omega t$	$\boldsymbol{8\pi(j-1)}$	$-20\pi/3(j-1)$
13	$14p\omega t$	$\boldsymbol{-12p\omega t}$	$28\pi/3(j-1)$	$\boldsymbol{-8\pi(j-1)}$
15	$16p\omega t$	$-14p\omega t$	$32\pi/3(j-1)$	$-28\pi/3(j-1)$
17	$\boldsymbol{18p\omega t}$	$-16p\omega t$	$\boldsymbol{12\pi(j-1)}$	$-32\pi/3(j-1)$
19	$20p\omega t$	$\boldsymbol{-18p\omega t}$	$40\pi/3(j-1)$	$\boldsymbol{-12\pi(j-1)}$
21	$22p\omega t$	$-20p\omega t$	$44\pi/3(j-1)$	$-40\pi/3(j-1)$
$\vdots$	$\vdots$	$\vdots$	$\vdots$	$\vdots$

TABLE 2. Model parameters.

Parameter	Symbol	Value	Unit
Number of pole-pair	p	$2,3,\cdots,50$	
Number of coil	$Q(=3p)$	$6,9,\cdots,150$	
Number of phase	q	3	(U,V,W)
Number of segment	l	$1,2,3,4$	
Slot-pitch	$\theta_s(\equiv 2\pi/Q)$		rad
Coil arc ratio	$\alpha(\equiv \theta_c/\theta_s)$		
Segment arc	$\Delta(\equiv \pi/(pl))$		rad
Inner radius of magnet	R_r	20,40,60,80	mm
Outer radius of magnet	R_m	40,100	mm
-	d	5	mm
Inner radius of yoke	$R_o(=R_r-d)$		mm
Outer radius of yoke	$R_s(=R_m+d)$		mm
Thickness of magnet	z_m	10	mm
Air-gap	g	0.5,1.0,1.5,2.0	mm
-	$z_s(\equiv z_m+g)$		
-	$\alpha_q(\equiv z_m/z_s)$		
-	$\tau(\equiv 2z_s)$		
Permeability of vacuum	μ_0	$4\pi\times 10^{-7}$	H/m
Remanent flux density	B_{rem}	1.34(N45M)	T
Coil turn	N_c	1	
Electric current	I_0	1	A
Angular frequency	ω	1	rad/s

where $\Theta_n \equiv \nu\theta_c/2$. The first term represents a uniform Lorentz torque independent of time, the second, third and fourth terms correspond to torque ripples of the 6th, 12th and 18th order harmonics, respectively. In a compact form, one can rewrite (69) as

$$\frac{1}{\mu_0 I_0 q}T = \sum_{k=1}^{\infty}\frac{(-1)^{k+1}}{\lambda}\mathscr{I}_{1k}\sin\Theta_1 + \sum_{m=1}^{\infty}\sum_{k=1}^{\infty}\frac{(-1)^{k+3m}}{\lambda} \times(\mathscr{I}_{6m-1,k}\sin\Theta_{6m-1}-\mathscr{I}_{6m+1,k}\sin\Theta_{6m+1}) \times\cos\phi_{6m-1}. \tag{70}$$

The torque constant K_t is defined as the uniform Lorentz torque T_0 per current as

$$K_t \equiv \frac{T_0}{I_0} = \mu_0 pq\sum_{k=1}^{\infty}\frac{(-1)^{k+1}}{\lambda}\mathscr{I}_{1k}\sin\Theta_1 \tag{71}$$

where T_0 corresponds to the first term of eq.(70).

IV. RESULTS AND DISCUSSION

A. VALIDITY OF ANALYTICAL MODEL

Main parameters adopted in this model are listed in Table 2. In order to validate the model, analytical results of the magnetic field distributions in the air-gap, back-EMF waveform and torque waveform are calculated by the use of the derived formulae (55), (60) and (69), respectively, and then compared with those of the FEM. The axial components B_z of the magnetic flux density at the central radius $r = R_c \equiv (R_r + R_m)/2$ and just below the upper yoke $z = z_s$ are plotted as a function of the azimuthal angle θ for some typical geometries of $p = 2$, 3 and 4 in Figs.4a), b) and c), respectively. The corresponding Fourier spectra are also drawn in Figs.4a′), b′) and c′), respectively. The magnetic field amplitudes $B_{z,n}$ are defined as $B_{z,n} \equiv \sum_k (-1)^{k+1}\lambda X_{2,nk}(x_c)$ with $x_c \equiv \lambda R_c$. It is shown that magnetic field distributions of $l = 1$ are almost the same irrespective of the number of poles, while those of $l = 2, 3, 4$ on the d-axis corresponding to $\theta = \pi/p$ gradually increase with an increase in poles. It is also found from the Fourier spectra that the fundamental amplitudes of the fields become strong with an increase in l except for the low-pole case a′), and that the space harmonics with $n = 2kl + 1 (k = 1, 2, \cdots)$ are excited for all cases. Specifically, the third harmonics appears only for the regular PM array. It would be expected from the spectra that the multipole-Halbach PM with $l = 4$ delivers the most superior performance in this study since the fundamental amplitude is the highest, and the harmonics is the lowest. The results of the analytical model for the magnetic field distributions and their Fourier spectra are in excellent agreement with those of the FEM.

In Fig.5, the axial components B_z in the air-gap on the d-axis corresponding to $\theta = 0$ are now plotted against the radial coordinate r for the same geometrical parameters as above. The magnetic field amplitudes increase in the order of $l = 1, 2, 3$ and 4, as is expected. More interestingly, their amplification of the fields becomes significant for higher poles. It should also be noted that the curves have a negative (right down) slope for $l \geq 2$ since the interaction of the magnetic fields in the Halbach PM is enhanced in the interior region. The analytical results agree well with the FEM ones except for some small deviations in the region close to the outer edge of the PM.

Temporal waveforms of the line back-EMF $\mathcal{E}_u - \mathcal{E}_v$ between the U- and V-phase and the relevant Lorentz torque T for the same parameters as above are shown in Figs.6 and 7, respectively. As l increases, the waveforms of the back-EMF approach sinusoidal irrespective of the number of poles. Simultaneously, the waveforms of the Lorentz torque shift upward decreasing their fluctuation, i.e torque ripple, for $p \geq 2$. However, amplitudes of the torque ripple increase with increasing the number of poles for all l. The observed improvement in the torque performance is consistent with the behavior of the Fourier spectra discussed above. It can be confirmed once again that the results of the analytical model agree well with those of the FEM.

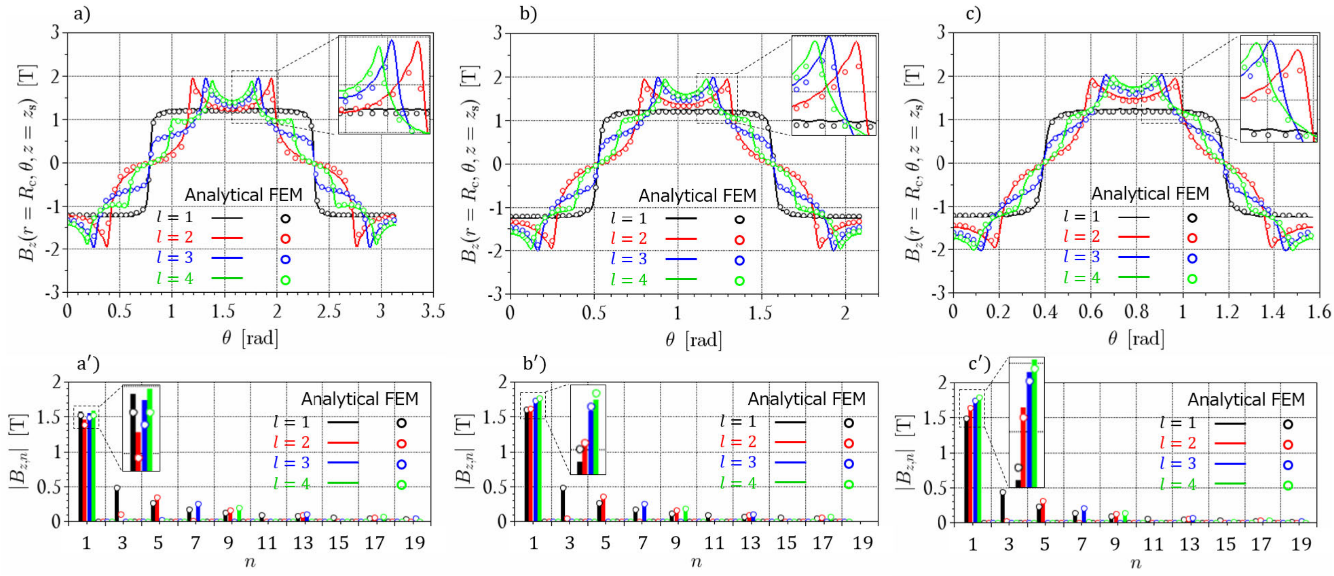

FIGURE 4. Axial components of the magnetic field against the azimuthal coordinate in the air-gap with $g = 0.5$ mm and $(R_r, R_m) = (20, 40)$ mm for a) $p = 2$, b) $p = 3$ and c) $p = 4$, and their corresponding Fourier spectra a′), b′) and c′), respectively. Dotted regions are separately enlarged for clarity of error.

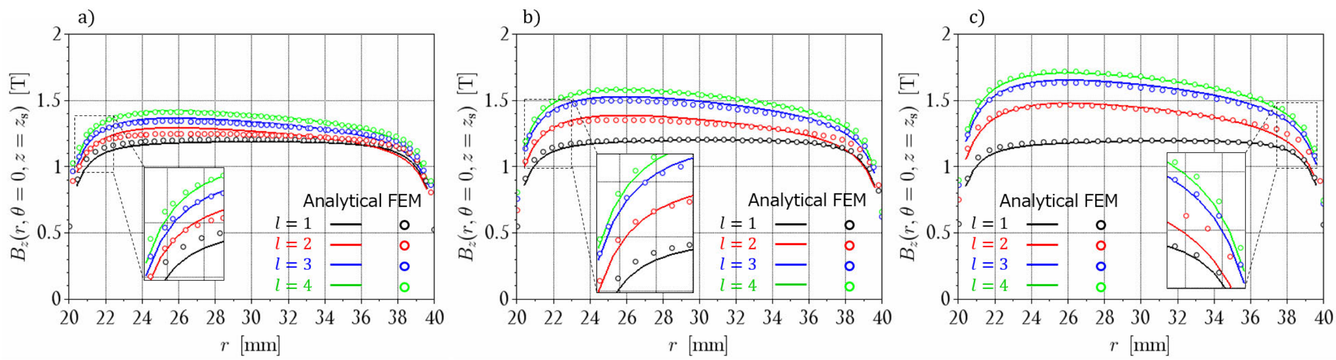

FIGURE 5. Axial components of the magnetic field against the radial coordinate in the air-gap with $g = 0.5$ mm and $(R_r, R_m) = (20, 40)$ mm for a) $p = 2$, b) $p = 3$ and c) $p = 4$. Dotted regions are separately enlarged for clarity of error.

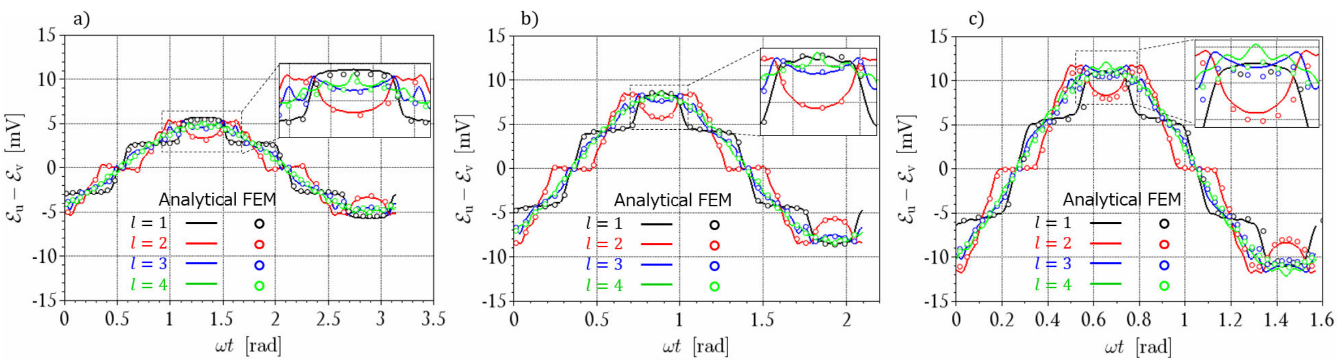

FIGURE 6. Waveforms of the line back-EMF with $g = 0.5$ mm and $(R_r, R_m) = (20, 40)$ mm for a) $p = 2$, b) $p = 3$ and c) $p = 4$. Dotted regions are separately enlarged for clarity of error.

Furthermore, the validity of the proposed model can well reasonably be explained by showing the fact that the mechanical output power $T\omega$ is identical with the electrical input power $\mathcal{E}_u I_u + \mathcal{E}_v I_v + \mathcal{E}_w I_w$. Namely, energy conservation law holds at anytime in the system of equations. It can be demonstrated not only numerically but also analytically that

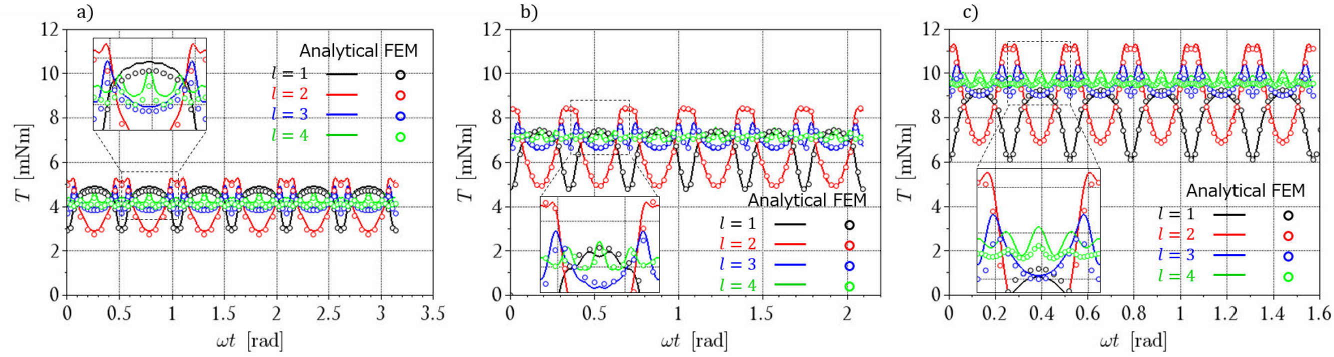

FIGURE 7. Waveforms of the Lorentz torque with $g = 0.5$ mm and $(R_r, R_m) = (20, 40)$ mm for a) $p = 2$, b) $p = 3$ and c) $p = 4$. Dotted regions are separately enlarged for clarity of error.

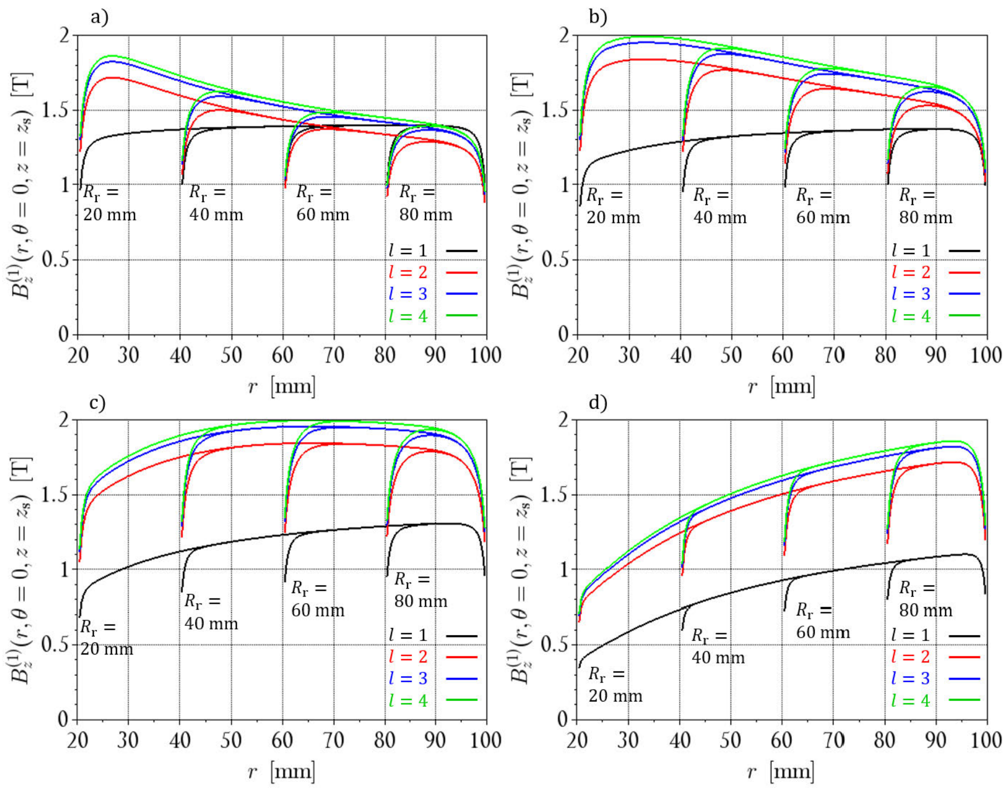

FIGURE 8. Axial components of the fundamental magnetic field against the radial coordinate in the air-gap with $g = 0.5$ mm for a) $p = 5$, b) $p = 10$, c) $p = 20$, and d) $p = 50$.

the expression for the Lorentz torque T given in (70) is consistently reproduced by calculating straightforwardly the formula $(\mathcal{E}_u I_u + \mathcal{E}_v I_v + \mathcal{E}_w I_w)/\omega$ with the aid of (59). Mathematical proof of the energy conservation law is presented in the Appendix C.

In the calculations of the FEM, commercial EM simulation software, JMAG-designer (x64) ver.21.0 [36] has been utilized on a high-end workstation equipped with a hexa-core processor. In this environment it takes 5 to 6 hours for the FEM, while only a few minutes for the analytical model to obtain a single waveform of the back-EMF or Lorentz torque.

B. RESULTS OF ANALYTICAL MODEL

Hereafter, discussion concentrates on the results obtained by the analytical model for globally parametrical study. In Fig.8, the axial components $B_z^{(1)}$ of the magnetic flux density with the fundamental mode ($n = 1$) on the d-axis are plotted against the radial coordinate r for a) $p = 5$, b) $p = 10$, c) $p = 20$ and d) $p = 50$, changing the inner radius $R_r = 20$, 40, 60 and 80 mm of the PM, respectively. As shown in Figs.8a) and b) for low-poles, the magnetic field with the regular PM of $l = 1$ is distributed almost uniformly except for both edges of the PM, while the fields with the Halbach

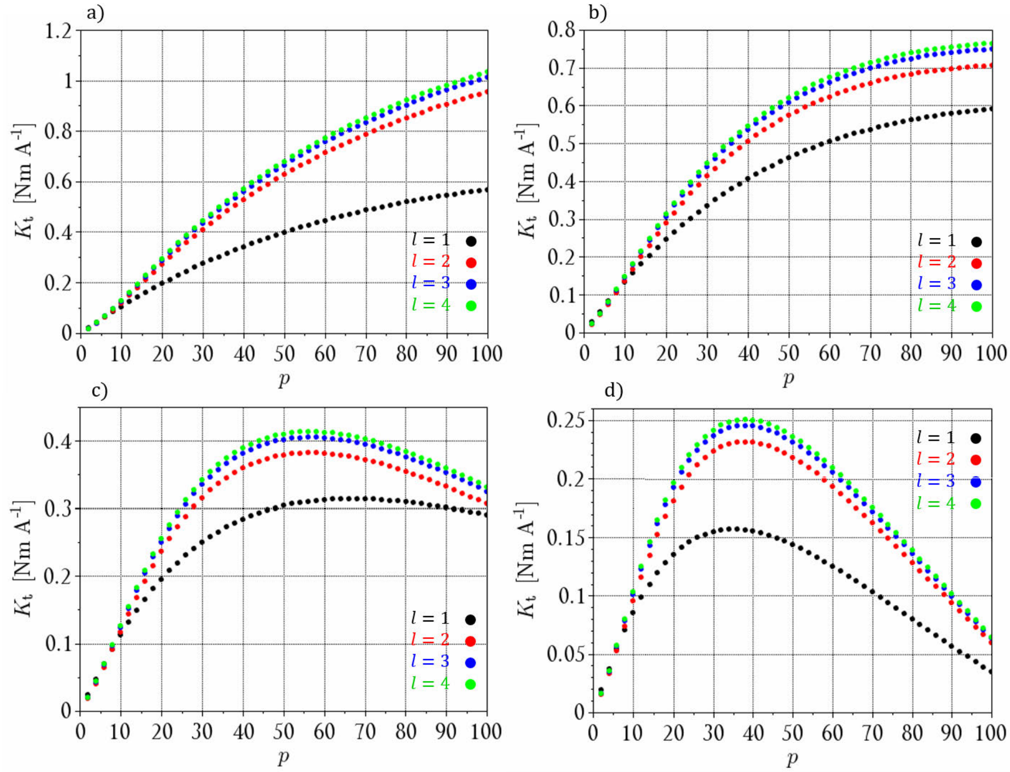

FIGURE 9. Torque constants against the number of pole-pairs with $R_r = 60$ mm and $R_m = 100$ mm of the magnet for a) $g = 0.5$ mm, b) $g = 1.0$ mm, c) $g = 1.5$ mm and d) $g = 2.0$ mm.

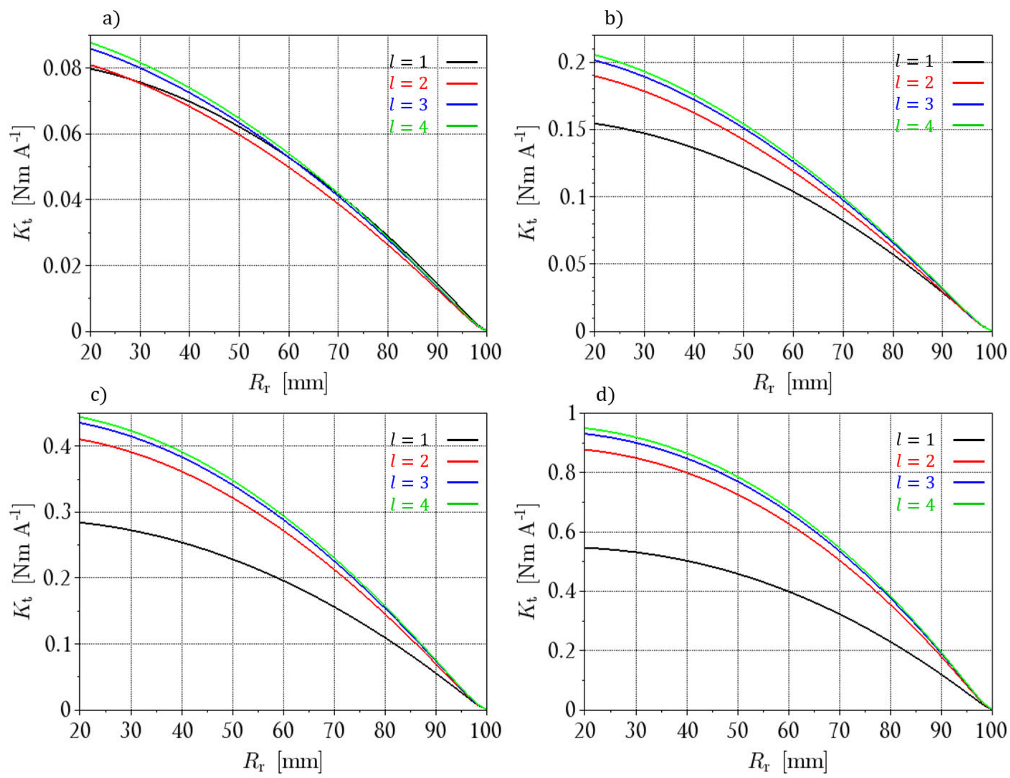

FIGURE 10. Torque constants against inner radius of the PM with $g = 0.5$ mm and $R_m = 100$ mm for a) $p = 5$, b) $p = 10$, c) $p = 20$ and d) $p = 50$.

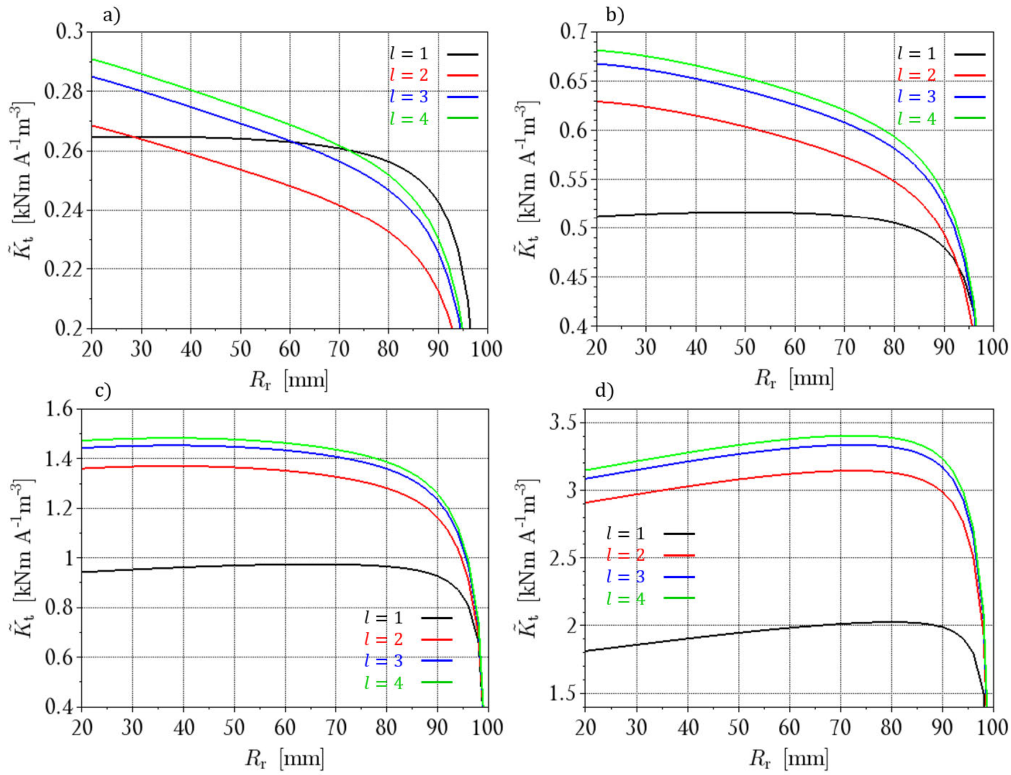

FIGURE 11. Torque constant densities against inner radius of the PM with $g = 0.5$ mm and $R_m = 100$ mm for a) $p = 5$, b) $p = 10$, c) $p = 20$ and d) $p = 50$.

PMs of $l = 2, 3$, and 4 increase inwardly irrespective of the values of the inner radii. While in c) for middle-poles, the fields are formed almost uniformly in a wide range of the radius for all l. In d) for high-poles, all of the fields increase outwardly contrary to the case a). It is found that the magnetic field structure in the radial direction strongly depends on the number of poles due to the convergence effect of the Halbach PM. It should be mentioned that the artificial correction function exploited in some preceding works would potentially overestimate or underestimate the magnetic field strength for low-poles and/or high-poles especially when the geometry of the AFPM is radially thick. The obtained results can be recognized by the fact that reducing R_r is intrinsically equivalent to increasing p and/or l because the distance between the neighboring PM segments close to the inner edge is estimated to be $R_r\pi/(pl)$.

In general, the torque constant of the RFPM machine is proportional to the product of the amplitude of the fundamental magnetic fields and the number of poles, i.e. $K_t \propto pB_\rho^{(1)}$, e.g., [37], where B_ρ is a radial component of the magnetic fields. On the other hand, the torque constant of the AFPM depends not only on the number of poles, but also on the radial structure of the magnetic fields through the integral term $\mathscr{I}_{1k}$ in (71). This is because the magnetic field in the air-gap of the RFPM is almost independent of the axial coordinate, while that of the AFPM is strongly dependent on the radial coordinate, as already shown in Fig.8. So now, Fig.9 shows the torque constants against the number of pole-pairs for some typical geometries of the AFPM with (R_r, R_m)=(60,100) mm for a) $g = 0.5$ mm, b) $g = 1.0$ mm, c) $g = 1.5$ mm and d) $g = 2.0$ mm. It is found that in the narrow air-gaps of a) and b) the torque constants monotonically increase with increasing p in the global range of $2 \leq p \leq 100$, while that in the large gaps of c) and d), maximum turning points clearly appear for all l.

In Fig.10, the torque constants are then plotted against the inner radius R_r of the PM with the fixed air-gap $g = 0.5$ mm and $R_m = 100$ mm for a) $p = 5$, b) $p = 10$, c) $p = 20$ and d) $p = 50$. For the low number of poles, significant difference among array-variables l cannot be found. However, for the high-poles $p \geq 10$ enhancement in the torque constant becomes more apparent because of the focusing effect of the multipole-Halbach PM as the number of poles increases, and/or as the inner radius of the PM decreases.

The torque constant per unit volume of the PM can be defined as $\tilde{K}_t \equiv K_t/\{\pi(R_m^2 - R_r^2)z_m\}$. Hereafter, $\tilde{K}_t$ is referred to as the torque constant density. Fig.11 presents the torque constant densities against the inner radius of the PM with $g = 0.5$ mm and $R_m = 100$ mm for a) $p = 5$, b) $p = 10$, c) $p = 20$ and d) $p = 50$. As shown in the figure, the torque constant densities increase with an increase in the number of poles, and become higher in the order of $l = 1, 2, 3$ and 4 except for the low-poles. Fig.11a) shows that the torque constant densities of the standard-Halbach PM are weaker than that of the regular PM since the focusing effect of the magnetic fields would be insufficient in almost the whole range of R_r.

For the middle-poles of b) and c), difference between the regular and multipole-Halbach PM becomes significant. For the high-poles of d), the torque constant densities keep high, but moderately decrease with decreasing inner radius for all l.

V. SUMMARY

The novel 3-D analytical model of the AFPM machine with a segmented multipole-Halbach PM array has been proposed in this paper. The mathematical expressions for magnetic fields, back-EMF, Lorentz torque and torque constant have successfully been derived in the explicit closed form, incorporating the effect of the space harmonics of the fields. Validity of the model can reasonably be demonstrated by the fact that the results obtained by the analytical model are in good agreement with those by the FEM, and that the law of energy conservation holds for the input- and output-power in the system of equations. On the basis of this model, the torque constant of the AFPM has been investigated in a wide range of the designing parameters, involving the number of poles, the number of segments per pole, air-gap and radius of the PM. The derived formulae and the obtained results are of much use in understanding the performance characteristics of the AFPM, and are available especially in early-designing of the electric machines, e.g. servomotors in multi-jointed robots or torque-controllable in-wheel AFPM machines on-board electric vehicles.

APPENDIX A: SOLUTION OF THE POISSON EQUATION

Poisson equation in the region Ω_2 is given in the form

$$\frac{\partial^2 X_{nk}}{\partial x^2} + \frac{1}{x}\frac{\partial X_{nk}}{\partial x} - \left(1 + \frac{\nu^2}{x^2}\right) X_{nk} = \mathcal{R} \tag{A-1}$$

where

$$\mathcal{R} \equiv \frac{1}{\lambda}\left(\frac{\nu M_{\theta nk}}{x} - M_{znk}\right). \tag{A-2}$$

Because independent solutions for the homogeneous differential equation with $\mathcal{R} = 0$ are $\varphi_\nu \equiv I_\nu(x)$ and $\psi_\nu \equiv K_\nu(x)$, general solution can be expressed as

$$X_{nk}^{(0)} = C_\nu \varphi_\nu(x) + D_\nu \psi_\nu(x) \tag{A-3}$$

While special solution for the inhomogeneous equation with $\mathcal{R} \neq 0$ can be written

$$X_{nk}^{(\mathrm{s})} = f_\nu(x)\varphi_\nu(x) + g_\nu(x)\psi_\nu(x) \tag{A-4}$$

where

$$f_\nu \equiv -\int dx \frac{\mathcal{R}\psi_\nu}{w} = \frac{1}{\lambda}\int dx(\nu M_{\theta nk} - M_{znk})\psi_\nu \tag{A-5}$$

$$g_\nu \equiv \int dx \frac{\mathcal{R}\varphi_\nu}{w} = -\frac{1}{\lambda}\int dx(\nu M_{\theta nk} - M_{znk})\psi_\nu \tag{A-6}$$

and

$$w \equiv \begin{vmatrix} \varphi_\nu & \psi_\nu \\ \varphi'_\nu & \psi'_\nu \end{vmatrix} = \varphi_\nu\psi'_\nu - \varphi'_\nu\psi_\nu = -\frac{1}{x} \tag{A-7}$$

is a Wronskians. Therefore, general solution for the inhomogeneous equation is given by

$$\begin{aligned} X_{nk} &= X_{nk}^{(0)} + X_{nk}^{(\mathrm{s})} \\ &= \{C_\nu + f_\nu(x)\}\varphi_\nu(x) + \{D_\nu + g_\nu(x)\}\psi_\nu(x). \end{aligned} \tag{A-8}$$

APPENDIX B: FOURIER COEFFICIENTS

In order to avoid overflow in the numerical integration involving Bessel's functions, the relevant coefficients C_{nk} and D_{nk} can respectively be modified to

$$\begin{aligned} C_{nk} &= \frac{-f_{nk,m} + \tilde{K}_{\nu,\mathrm{s}}\tilde{I}_{\nu,\mathrm{s}}^{-1} g_{nk,\mathrm{m}}}{1 - \tilde{K}_{\nu,\mathrm{s}}\tilde{I}_{\nu,\mathrm{s}}^{-1}\tilde{I}_{\nu,\mathrm{o}}\tilde{K}_{\nu,\mathrm{o}}^{-1}} \\ &= \frac{-f_{nk,\mathrm{m}} + \epsilon g_{nk,\mathrm{m}}}{1-\delta} \\ &\simeq (-f_{nk,\mathrm{m}} + \epsilon g_{nk,\mathrm{m}})(1+\delta) \\ &= -f_{nk,\mathrm{m}} + \epsilon g_{nk,\mathrm{m}} - \delta f_{nk,\mathrm{m}} + \mathrm{O}(\epsilon^2, \delta^2, \epsilon\delta) \end{aligned} \tag{B-1}$$

and

$$\begin{aligned} D_{nk} &= \frac{\tilde{I}_{\nu,\mathrm{o}}\tilde{K}_{\nu,\mathrm{o}}^{-1}(-f_{nk,\mathrm{m}} + \tilde{K}_{\nu,\mathrm{s}}\tilde{I}_{\nu,\mathrm{s}}^{-1} g_{nk,\mathrm{m}})}{1 - \tilde{K}_{\nu,\mathrm{s}}\tilde{I}_{\nu,\mathrm{s}}^{-1}\tilde{I}_{\nu,\mathrm{o}}\tilde{K}_{\nu,\mathrm{o}}^{-1}} \\ &= \tilde{I}_{\nu,\mathrm{o}}\tilde{K}_{\nu,\mathrm{o}}^{-1} C_{nk} \end{aligned} \tag{B-2}$$

with $\epsilon \equiv \tilde{K}_{\nu,\mathrm{s}}\tilde{I}_{\nu,\mathrm{s}}^{-1}$ and $\delta \equiv \tilde{I}_{\nu,\mathrm{o}}K_{\nu,\mathrm{o}}^{-1}\epsilon$

APPENDIX C: ENERGY CONSERVATION

It can mathematically be demonstrated on the basis of the derived formulae for the back-EMF and the torque that the law of energy conservation $T\omega = \mathcal{E}_\mathrm{u}I_\mathrm{u} + \mathcal{E}_\mathrm{v}I_\mathrm{v} + \mathcal{E}_\mathrm{w}I_\mathrm{w}$ holds at anytime in the system. Electrical input power P_in^e can be expressed by

$$P_\mathrm{in}^\mathrm{e} \equiv \sum_{j=1}^{q} \mathcal{E}_j I_j \tag{C-1}$$

where

$$\begin{aligned} \mathcal{E}_j &= -\frac{\partial \Phi_j}{\partial t} \\ &= -2\mu_0\omega \sum_{n=\mathrm{odd}}^{\infty}\sum_{k=1}^{\infty} \frac{(-1)^{k+1}}{\lambda}\mathscr{I}_{nk}\sin\Theta_n \\ &\quad \times \sin\nu(\theta_j - \omega t) \end{aligned} \tag{C-2}$$

$$I_j = I_0\cos p(\omega t - \delta_j) \tag{C-3}$$

with $\delta_j = 2\pi(j-1)/(pq)$ and $\theta_j = \theta_\mathrm{s}(j-1) + \pi/(2p)$. Using the trigonometric identity, one obtains

$$\begin{aligned} &2\sum_{j=1}^{q}\sin\nu(\theta_j - \omega t)\cos p(\omega t - \delta_j) \\ &= (-1)^{\frac{n-1}{2}}\cos p(n+1)\omega t\sum_{j=1}^{q}\cos\varpi_{nj}^{+} \end{aligned}$$

$$-(-1)^{\frac{n+1}{2}} \sin p(n+1)\omega t \sum_{j=1}^{q} \sin \varpi_{nj}^{+}$$
$$+(-1)^{\frac{n-1}{2}} \cos p(n-1)\omega t \sum_{j=1}^{q} \cos \varpi_{nj}^{-}$$
$$-(-1)^{\frac{n+1}{2}} \sin p(n-1)\omega t \sum_{j=1}^{q} \sin \varpi_{nj}^{-} \quad \text{(C-4)}$$

with $\varpi_{nj}^{\pm} \equiv 2\pi(n\pm1)(j-1)/3$. The terms of summation with respect to j can be dropped or simplified into the form

$$\sum_{j=1}^{q} \sin \varpi_{nj}^{\pm} = 0 \quad \text{(C-5)}$$
$$\sum_{j=1}^{q} \cos \varpi_{nj}^{+} = q\delta_{n,6m-1}\ (m = 1, 2, 3, \cdots) \quad \text{(C-6)}$$
$$\sum_{j=1}^{q} \cos \varpi_{nj}^{-} = q\delta_{n,6m'+1}\ (m' = 0, 1, 2, \cdots) \quad \text{(C-7)}$$

where $\delta_{nm} = 1$ $(n = m)$ or 0 $(n \neq m)$ is a Kronecker delta notation. Substitution of (C.2) and (C.3) into (C.1) with the help of (C.5)-(C.7) leads to the following formula

$$\frac{P_{\text{in}}^{\text{e}}}{\mu_0 q I_0 \omega} = \sum_{m=1}^{\infty}\sum_{k=1}^{\infty} \frac{(-1)^{\frac{2k+n+3}{2}}}{\lambda} \mathscr{I}_{nk} \sin\Theta_n \cos p(n+1)\omega t \delta_{n,6m-1}$$
$$- \sum_{m'=0}^{\infty}\sum_{k=1}^{\infty} \frac{(-1)^{\frac{2k+n+1}{2}}}{\lambda} \mathscr{I}_{nk} \sin\Theta_n \cos p(n-1)\omega t \delta_{n,6m'+1}. \quad \text{(C-8)}$$

It is found from this result that the fundamental mode $n = 1$ originates from $m' = 0$ only. The above formula can therefore be rewritten in the separation form between the fundamental $m' = 0$ and the harmonic modes $m' = m = 1, 2, \cdots$

$$\frac{P_{\text{in}}^{\text{e}}}{\mu_0 q I_0 \omega} = \sum_{m=1}^{\infty}\sum_{k=1}^{\infty} \frac{(-1)^{\frac{2k+n+3}{2}}}{\lambda} \mathscr{I}_{nk} \sin\Theta_n \cos p(n+1)\omega t \delta_{n,6m-1}$$
$$- \sum_{k=1}^{\infty} \frac{(-1)^{k+1}}{\lambda} \mathscr{I}_{1k} \sin\Theta_1$$
$$- \sum_{m=1}^{\infty}\sum_{k=1}^{\infty} \frac{(-1)^{\frac{2k+n+1}{2}}}{\lambda} \mathscr{I}_{nk} \sin\Theta_n \cos p(n-1)\omega t \delta_{n,6m+1}. \quad \text{(C-9)}$$

The electrical input power can finally be given in the following expression

$$\frac{P_{\text{in}}^{\text{e}}}{\mu_0 q I_0 \omega} = -\sum_{k=1}^{\infty} \frac{(-1)^{k+1}}{\lambda} \mathscr{I}_{1k} \sin\Theta_1$$
$$- \sum_{m=1}^{\infty}\sum_{k=1}^{\infty} \frac{(-1)^{k+3m}}{\lambda}$$
$$\times (\mathscr{I}_{6m-1,k} \sin\Theta_{6m-1} - \mathscr{I}_{6m+1,k} \sin\Theta_{6m+1})$$
$$\times \cos 6mp\omega t. \quad \text{(C-10)}$$

This formula exactly coincides with the mechanical output power $P_{\text{out}}^{\text{m}} \equiv T\omega$.

ACKNOWLEDGMENT

The authors would like to thank the Head of the Research and Development Institute for permitting the publication of this work.

REFERENCES

[1] J. M. Seo, S. Rhyu, J. Kim, J. Choi, and I. Jung, "Design of axial flux permanent magnet brushless DC motor for robot joint module," in *Proc. IEEE Int. Elect. Conf.*, Sapporo, Japan, Jun. 2010, pp. 1336–1340.

[2] R. Huang, Z. Song, Z. Dong, Y. Liu, and C. Liu, "Design of a new double side axial-flux actuator for robot dog," in *Proc. Int. Conf. Electr. Mach. (ICEM)*, Sep. 2022, pp. 900–906.

[3] D.-Y. Shin, M.-J. Jung, K.-B. Lee, K.-D. Lee, and W.-H. Kim, "A study on the improvement of torque density of an axial slot-less flux permanent magnet synchronous motor for collaborative robot," *Energies*, vol. 15, no. 9, p. 3464, May 2022.

[4] *Genesis Robotics & Motion Technologies*. Accessed: Dec. 2022. [Online]. Available: https://genesisrobotics.com

[5] Y. P. Yang, C. H. Lee, and P. C. Hung, "Multi-objective optimal design of an axial-flux permanent-magnet wheel motor for electric scooters," *IET Electr. Pow. Appl.*, vol. 8, pp. 1–12, Oct. 2013.

[6] W. Deng and S. Zuo, "Analytical modeling of the electromagnetic vibration and noise for an external-rotor axial-flux in-wheel motor," *IEEE Trans. Ind. Electron.*, vol. 65, no. 3, pp. 1991–2000, Mar. 2018.

[7] K.-H. Kim and D.-K. Woo, "Novel quasi-three-dimensional modeling of axial flux in-wheel motor with permanent magnet skew," *IEEE Access*, vol. 10, pp. 98842–98854, 2022.

[8] W. Geng, Y. Wang, J. Wang, J. Hou, J. Guo, and Z. Zhang, "Comparative study of yokeless stator axial-flux PM machines having fractional slot concentrated and integral slot distributed windings for electric vehicle traction applications," *IEEE Trans. Ind. Electron.*, vol. 70, no. 1, pp. 155–166, Jan. 2023.

[9] A. S. Holmes, G. Hong, and K. R. Pullen, "Axial-flux permanent magnet machines for micropower generation," *J. Microelectromech. Syst.*, vol. 14, no. 1, pp. 54–62, Feb. 2005.

[10] P. Virtič, P. Pišek, T. Marčič, M. Hadžiselimovič, and B. Štumberger, "Analytical analysis of magnetic field and back electromotive force calculation of an axial-flux permanent magnet synchronous generator with coreless stator," *IEEE Trans. Magn.*, vol. 44, no. 11, pp. 4333–4336, Nov. 2008.

[11] H. Gorginpour, "Analysis and design considerations of an axial-flux dual-rotor consequent-pole Vernier-PM machine for direct-drive energy conversion systems," *IET Renew. Power Gener.*, vol. 14, no. 2, pp. 211–221, Feb. 2020.

[12] M. A. Noroozi Dehdez and J. Milimonfared, "A novel radial–axial flux switching permanent magnet generator," *IEEE Trans. Ind. Electron.*, vol. 69, no. 12, pp. 12096–12106, Dec. 2022.

[13] *Massachusetts Institute Of Technology*. Accessed: Dec. 2022. [Online]. Available: https://web.mit.edu

[14] *Carnegie Mellon University, the Robotics Institute*. Accessed: Dec. 2022. [Online]. Available: https://www.ri.cmu.edu

[15] *ABB*. Accessed: Dec. 2022. [Online]. Available: https://global.abb

[16] *EPSON*. Accessed: Dec. 2022. [Online]. Available: https://global.epson.com

[17] *KUKA*. Accessed: Dec. 2022. [Online]. Available: https://www.kuka.com

[18] K. Halbach, "Design of permanent multipole magnets with oriented rare earth cobalt material," *Nucl. Instrum. Methods*, vol. 169, no. 1, pp. 1–10, Feb. 1980.

[19] Z. Q. Zhu, Z. P. Xia, K. Atallah, G. W. Jewell, and D. Howe, "Analytical of anisotropic bonded NdFeB Halbach cylinders accounting for partial powder alignment," *IEEE Trans. Magn.*, vol. 36, no. 5, pp. 3575–3577, Sep. 2000.

[20] Y. Shen and Z. Q. Zhu, "Analysis of electromagnetic performance of Halbach PM brushless machines having mixed grade and unequal height of magnets," *IEEE Trans. Magn.*, vol. 49, no. 4, pp. 1461–1469, Apr. 2013.

[21] R. Bjørk, A. Smith, and C. R. H. Bahl, "Analysis of the magnetic field, force, and torque for two-dimensional Halbach cylinders," *J. Magn. Magn. Mater.*, vol. 322, no. 1, pp. 133–141, Jan. 2010.
[22] D. Mansson, "On the optimization of Halbach arrays as energy storage media," *Prog. Electromagn. Res. B*, vol. 62, pp. 277–288, 2015.
[23] C. Wang, Z. Zhang, Y. Liu, W. Geng, and H. Gao, "Effect of slot-pole combination on the electromagnetic performance of ironless stator AFPM machine with concentrated windings," *IEEE Trans. Energy Convers.*, vol. 35, no. 2, pp. 1098–1109, Jun. 2020.
[24] M. Lee, B. Koo, and K. Nam, "Analytic optimization of the Halbach array slotless motor considering stator yoke saturation," *IEEE Trans. Magn.*, vol. 57, no. 2, pp. 1–6, Feb. 2021.
[25] G. D. Donato, F. G. Capponi, G. A. Rivellini, and F. Caricchi, "Integral-slot versus fractional-slot concentrated-winding axial-flux permanent-magnet machines: Comparative design, FEA, and experimental tests," *IEEE Trans. Ind. Appl.*, vol. 48, no. 5, pp. 1487–1495, Sep. 2012.
[26] E. Cetin and F. Daldaban, "Analyzing distinctive rotor poles of the axial flux PM motors by using 3D-FEA in view of the magnetic equivalent circuit," *Eng. Sci. Technol., Int. J.*, vol. 20, no. 5, pp. 1421–1429, Oct. 2017.
[27] R. Huang, C. Liu, Z. Song, and H. Zhao, "Design and analysis of a novel axial-radial flux permanent magnet machine with Halbach-array permanent magnets," *Energies*, vol. 14, no. 12, p. 3639, Jun. 2021.
[28] E. P. Furlani, "A method for predicting the fields in axial field motors," *IEEE Trans. Magn.*, vol. 28, no. 5, pp. 2061–2066, Sep. 1992.
[29] E. P. Furlani and M. A. Knewtson, "A three-dimensional field solution for permanent-magnet axial-field motors," *IEEE Trans. Magn.*, vol. 33, no. 3, pp. 2322–2325, May 1997.
[30] Y. N. Zhilichev, "Calculation of 3D magnetic field of disk-type micromotors by integral transformation method," *IEEE Trans. Magn.*, vol. 32, no. 1, pp. 248–253, Jan. 1996.
[31] S. Y. Sung, J. H. Jeong, Y. S. Park, J. Y. Choi, and S. M. Jang, "Improved analytical modeling of axial flux machine with a double-sided permanent magnet rotor and slotless stator based on an analytical method," *IEEE Trans. Magn.*, vol. 48, no. 11, pp. 2945–2948, Nov. 2012.
[32] H.-J. Shin, J.-Y. Choi, H.-W. Cho, and S.-M. Jang, "Analytical torque calculations and experimental testing of permanent magnet axial eddy current brake," *IEEE Trans. Magn.*, vol. 49, no. 7, pp. 4152–4155, Jul. 2013.
[33] O. De La Barriere, S. Hlioui, H. B. Ahmed, M. Gabsi, and M. LoBue, "3-D formal resolution of Maxwell equations for the computation of the no-load flux in an axial flux permanent-magnet synchronous machine," *IEEE Trans. Magn.*, vol. 48, no. 1, pp. 128–136, Jan. 2012.
[34] Y. Huang, B. Ge, J. Dong, H. Lin, J. Zhu, and Y. Guo, "3-D analytical modeling of no-load magnetic field of ironless axial flux permanent magnet machine," *IEEE Trans. Magn.*, vol. 48, no. 11, pp. 2929–2932, Nov. 2012.
[35] P. Jin, Y. Yuan, Q. Xu, S. Fang, H. Lin, and S. L. Ho, "Analysis of axial-flux Halbach permanent-magnet machine," *IEEE Trans. Magn.*, vol. 51, no. 11, pp. 1–4, Nov. 2015.
[36] *JMAG*. Accessed: Dec. 2022. [Online]. Available: https://www.jmag-international.com
[37] J. Pyrhonen, T. Jokinen, and V. Hrabovcova, *Design of Rotating Electrical Machines*, 2nd ed. Hoboken, NJ, USA: Wiley, 2013.

TAISHI OKITA received the Ph.D. degree in physics from Hiroshima University, Japan, in 2006. He was a Postdoctoral Research Fellow with the Research Institute for Fundamental Physics, Kyoto University, from 2006 to 2008, and the Institute of Fluid Science, Tohoku University, from 2008 to 2010. He was a Visiting Research Fellow with TOYOTA Central Research and Development Laboratories Corporation, from 2010 to 2012, a Visiting Researcher with Japan Aerospace Exploration Agency, from 2012 to 2013, and a Chief Researcher with Samsung Electro-Mechanics Corporation, from 2014 to 2015. Currently, he is a Senior Researcher with the Research and Development Department, Seiko Epson Corporation, where he is engaged in the research of electric machines for robots and mobility. His specialized area includes electromagnetic field theory.

HISAKO HARADA received the M.E. degree in engineering from the Graduate School of Science and Technology, Chiba University, Japan, in 2002. Since 2002, she has been working as a Research Engineer with Seiko Epson Corporation. Currently, she is a Senior Researcher with the Research and Development Department, where she is engaged in the electromagnetic field simulation of electric machines.